APS physics

CHORUS

This is the accepted manuscript made available via CHORUS. The article has been published as:

# Ferromagnetic resonance and control of magnetic anisotropy by epitaxial strain in the ferromagnetic semiconductor $(Ga_{0.8},Fe_{0.2})Sb$ at room temperature

Shobhit Goel, Le Duc Anh, Shinobu Ohya, and Masaaki Tanaka

Phys. Rev. B **99**, 014431 — Published 25 January 2019

DOI: 10.1103/PhysRevB.99.014431

# Ferromagnetic resonance and control of magnetic anisotropy by epitaxial strain in ferromagnetic semiconductor $(Ga_{0.8},Fe_{0.2})Sb$ at room temperature

Shobhit Goel,[1,#] Le Duc Anh,[1,2,*] Shinobu Ohya,[1,2,3,+] and Masaaki Tanaka[1,3,†]

[1]*Department of Electrical Engineering and Information Systems, The University of Tokyo, 7-3-1 Hongo, Bunkyo-ku, Tokyo 113-8656, Japan*
[2]*Institute of Engineering Innovation, The University of Tokyo, 7-3-1 Hongo, Bunkyo-ku, Tokyo 113-8656, Japan*
[3]*Center for Spintronics Research Network (CSRN), The University of Tokyo, 7-3-1 Hongo, Bunkyo-ku, Tokyo 113-8656, Japan*

**Abstract**

We study the strain dependence of the magnetic anisotropy of room-temperature ferromagnetic semiconductor $(Ga_{1-x},Fe_x)Sb$ ($x$ = 20%) thin films epitaxially grown on different buffer layers, using ferromagnetic resonance measurements. We show that the magnetocrystalline anisotropy ($K_i$) in $(Ga_{1-x},Fe_x)Sb$ exhibits a dependence on the epitaxial strain and changes its sign from negative (in-plane magnetization easy axis) to positive (perpendicular magnetization easy axis), when the strain is changed from tensile to compressive. Meanwhile, the shape anisotropy ($K_{sh}$) is negative and dominant over $K_i$. Therefore, the effective magnetic anisotropy ($K_{eff} = K_i + K_{sh}$) is always negative, leading to the in-plane magnetic anisotropy in all the $(Ga_{1-x},Fe_x)Sb$ samples. This work is the first observation of ferromagnetic resonance and strong shape anisotropy at room temperature in III-V ferromagnetic semiconductors. We also observed very high Curie temperature ($T_C \gtrsim 400$ K) in *p*-type (Ga,Fe)Sb, which is the highest $T_C$ reported so far in III-V based ferromagnetic semiconductors.

[#] goel@cryst.t.u-tokyo.ac.jp
[*] anh@cryst.t.u-tokyo.ac.jp
[+] ohya@cryst.t.u-tokyo.ac.jp
[†] masaaki@ee.t.u-tokyo.ac.jp

## I. Introduction

Ferromagnetic semiconductors (FMSs) have attracted much attention since they exhibit both semiconducting and ferromagnetic properties, which provide a straightforward approach for integrating spin-dependent phenomena into semiconductor devices. From FMS thin films, one can inject a spin-polarized current into a nonmagnetic semiconductor using methods such as electrical spin injection [1]–[4] and spin-pumping [4], without suffering from severe problems such as conductivity mismatch and interface roughness as seen in general ferromagnetic metal-semiconductor contacts [1],[2]. This good compatibility with conventional semiconductor technology is very important for the realization of semiconductor spintronic devices with nonvolatile functions and low power dissipation [6]–[11]. Thus far, the mainstream studies of FMSs are based on the Mn-doped III-V FMSs such as (Ga,Mn)As. These Mn-doped FMSs, however, maintain ferromagnetic order only at low temperature (the highest Curie temperature $T_C$ is 200 K in (Ga,Mn)As [12]) and they have strong crystalline anisotropy, which results in a difficulty to control the magnetization by nano-fabrication processing. Besides, Mn-doped FMSs are only *p*-type, because Mn acts as an acceptor in III-V semiconductors. These are severe drawbacks that hinder the use of FMSs in practical spintronic devices.

Recently, we found that Fe-doped narrow-gap III-V FMSs can be promising alternatives to overcome the problems of the Mn-based FMSs. By using Fe as the magnetic dopants, one can grow both *n*-type FMSs ((In,Fe)As [13]–[15], (In,Fe)Sb [16]) and *p*-type FMSs ((Al,Fe)Sb [17], (Ga,Fe)Sb [18],[19]), because Fe atoms are in the isoelectronic $Fe^{3+}$ state and do not supply carriers. The most notable feature in the Fe-doped FMSs is their very high $T_C$: Intrinsic room-temperature ferromagnetism has been confirmed in $(Ga_{1-x},Fe_x)Sb$ thin films with the Fe density $x$

$\geq$ 23% [18], and in $(In_{1-x},Fe_x)Sb$ thin films with $x \geq 16\%$ [16]. Therefore, these new Fe-doped FMSs are expected to be useful materials for spintronic device applications at room temperature.

In this paper, we study the growth and magnetic anisotropy (MA) of $(Ga_{1-x},Fe_x)Sb$ ($x = 0.2$) thin films epitaxially grown on different buffer layers and thus subjected to different epitaxial strains. MA plays an important role in controlling the magnetization of the ferromagnetic (FM) thin films, which is a fundamental operation of magnetic/spintronic devices. Understanding and controlling the MA, thus, are essential for device applications of (Ga,Fe)Sb. In the past, researchers successfully observed and controlled the MA of the III-V Mn-doped FMSs, (Ga,Mn)As [20]–[27] and (In,Mn)As [29]–[31] ferromagnetic thin films, by epitaxial strain. These Mn-doped FMSs showed a perpendicular-magnetization easy axis under tensile strain, and an in-plane-magnetization easy axis under compressive strain. In this work, we have grown $(Ga_{1-x},Fe_x)Sb$ thin films on four different buffer layers (AlSb, GaSb, $In_{0.5}Ga_{0.5}As$, and GaAs) by molecular beam epitaxy (MBE) to induce different epitaxial strains ranging from tensile to compressive, and examined its effect on the MA of these $(Ga_{1-x},Fe_x)Sb$ thin films.

We performed ferromagnetic resonance (FMR) measurements to investigate the MA fields of the $(Ga_{1-x},Fe_x)Sb$ thin films. FMR is not only one of the most efficient and powerful techniques to observe the MA [32], but also used for spin pumping to inject spin angular momentum (spin current) from an FM material into nonmagnetic metals and semiconductors. Therefore, observing FMR in the (Ga,Fe)Sb thin films, particularly at room temperature, is a fundamental and important step to study this material as a spin injector in practical spin devices. Here, we measured the dependence of the FMR resonance field on the external magnetic-field direction and fitted a theoretical curve to the data to obtain the MA fields of the (Ga,Fe)Sb thin films. We performed careful analyses of the MA to separate the shape anisotropy ($K_{sh}$), which is due to the

dipole-dipole interactions, and the magnetocrystalline anisotropy ($K_i$), which is due to the spin-orbit interactions, and discussed the effect of epitaxial strain on these two components.

## II. Sample growth and characterizations

We have grown a series of four samples A–D of *p*-type FMS (Ga,Fe)Sb thin films on semi-insulating GaAs (001) substrates by low temperature molecular beam epitaxy (LT-MBE), whose growth parameters are given in Table I. The schematic structure of our samples is shown in Fig. 1(a). In samples A, B, and C, on a semi-insulating GaAs (001) substrate we first grew a 100-nm-thick GaAs layer at a substrate temperature $T_S$ = 550 $^oC$ to obtain an atomically flat surface, next we grew a 10-nm-thick AlAs layer at the same $T_S$. Then, we grew a thick buffer layer, which is a 300-nm-thick AlSb layer at $T_S$ = 470 $^oC$ for sample A, a 300-nm-thick GaSb layer at $T_S$ = 470 $^oC$ for sample B, and a 500-nm-thick $In_{0.5}Ga_{0.5}As$ layer at $T_S$ = 550 $^oC$ for sample C. For sample D, a 500-nm-thick GaAs buffer layer was grown directly on a semi-insulating GaAs (001) substrate at $T_S$ = 550 $^oC$. Finally, we grew a 15-nm-thick $(Ga_{1-x},Fe_x)Sb$ layer with an Fe concentration $x$ = 20% at a growth rate of 0.5 μm/h and an Sb cracker cell pressure of $7.8 \times 10^{-5}$ Pa at $T_S$ = 250 $^oC$ for all the samples. As shown in Fig. 1(c), *in-situ* reflection-high energy electron diffraction (RHEED) patterns in the $[\bar{1}10]$ direction of the (Ga,Fe)Sb thin films in all the four samples are bright and streaky, thereby indicating good two-dimensional growth of a zinc-blende crystal structure. In this way, we obtained high-quality (Ga,Fe)Sb thin films, whose quality is better than that of our previous reports [18],[19], because we optimized the MBE growth conditions: The properties of (Ga,Fe)Sb depends on the Sb pressure during the MBE growth and we found that by keeping a higher $Sb_4$ pressure at $7.8 \times 10^{-5}$ Pa in the MBE growth chamber before Ga and Fe

fluxes were supplied, we obtained high $T_C$ > 300K in $(Ga_{1-x},Fe_x)Sb$ with an lower Fe concentration of $x$ = 20% (this is an improvement from our previous reports [18],[19]).

We characterized the crystal structures and lattice constants of all the (Ga,Fe)Sb thin films and buffer layers by x-ray diffraction (XRD). Figures 2(a) –2(d) show the XRD results of samples A–D, respectively. All the samples show a sharp GaAs (004) peak. In samples A, B, and C, there is a broader peak which can be deconvoluted into two Gaussian peaks corresponding to the buffer layer and (Ga,Fe)Sb (004). In sample D, the (Ga,Fe)Sb (004) peak can be clearly seen. From the peak positions, we estimated the intrinsic lattice constants of (Ga,Fe)Sb ($a_{GaFeSb}$) and of the buffer layer ($a_{buffer}$) [33]. We define the epitaxial strain $\varepsilon$ as $\frac{a_{GaFeSb}-a_{buffer}}{a_{GaFeSb}}\times 100$ (%). As listed in Table I, the estimated values of $\varepsilon$ indicate that the (Ga,Fe)Sb films can have both tensile and compressive strains when they are grown on different buffer layers. Here, samples A ($\varepsilon$ = –1.7%, AlSb buffer layer) and B ($\varepsilon$ = –0.1%, GaSb buffer layer) have tensile strain, whereas samples C ($\varepsilon$ = 0.23%, $In_{0.5}Ga_{0.5}As$ buffer layer) and D ($\varepsilon$ = 3.84%, GaAs buffer layer) have compressive strain. These results demonstrate that we can systematically vary the epitaxial strain of (Ga,Fe)Sb in a wide range, from tensile to compressive, by growing it on appropriate buffer layers.

Next, we characterized the magnetic properties of all the samples using magnetic circular dichroism (MCD) spectroscopy and superconducting quantum interference device (SQUID) magnetometry. As shown in Figs. 3(a)–3(h), the magnetic-field dependences of MCD (MCD – $H$ curves) show clear hysteresis, and the Arrott plots indicate that $T_C$ is higher than 320 K in all the samples. To estimate the exact value of $T_C$, we measured remanent magnetization versus temperature ($M$ –$T$) curves up to 400 K [33]. It is shown that the remanent magnetization is still present even at 400 K. We have also measured magnetization hysteresis ($M$ – $H$) curves at 400 K

as shown in Figs. 4(a)–4(d), in which we can see clear remanent magnetization. Therefore, $T_C$ is higher than 400 K. These results prove that the room-temperature ferromagnetism is obtained in all the four (Ga,Fe)Sb samples with the Fe concentration of 20%.

Figures 5(a)–5(d) show the magnetic-field dependence of the magnetization ($M - H$) of $(Ga_{0.8},Fe_{0.2})Sb$ measured for samples A–D at 50 K, with a magnetic field $\boldsymbol{H}$ applied along the in-plane [110] axis (solid circles) and the perpendicular [001] axis (open circles). In all the samples, $M$ saturates with smaller $H$ when $\boldsymbol{H}$ // [110] than when $\boldsymbol{H}$ // [001]. These results show that the easy magnetization axes of the (Ga,Fe)Sb thin films lie in the in-plane direction in all the four samples regardless of the different epitaxial strains. We note that the same results were obtained from the $M - H$ curves measured using SQUID at room temperature. Also, we observed a tendency that the saturation magnetization decreases with increasing $\varepsilon$, which can be attributed to the degradation of the crystal quality of the films due to the buffer layer. The crystal quality change is observed in the linewidths in the ferromagnetic resonance (FMR) spectra, which is discussed in Section III.

## III. Experimental setup of ferromagnetic-resonance (FMR) measurements and theoretical model

We used a Bruker electron paramagnetic resonance (EPR) spectrometer for performing FMR measurements at 9.066 GHz. As shown in Fig. 1(b), in our FMR measurements, the microwave radio frequency (rf) magnetic field ($h$) is applied along the $[\bar{1}10]$ axis in the film plane and the direct-current (dc) magnetic field $\boldsymbol{H}$ is rotated from the [110] direction (in the film plane) to the [001] direction (perpendicular to the film plane). Initially, we cut the sample into a 3×1 mm size

piece with edges along $[\bar{1}10]$ (3 mm) and $[110]$ (1 mm). Then, we put it on the center of a quartz sample rod and placed it inside the center of the microwave cavity that resonates in the $TE_{011}$ mode, where $h$ and rf electric field ($e$) are largest and smallest, respectively. The FMR spectrum was then measured by sweeping the magnitude of $\boldsymbol{H}$. The magnetic-field derivative of the microwave absorption was obtained by superimposing an alternating-current (ac) magnetic field $\boldsymbol{H}_{ac}$ (1 mT, 100 kHz) parallel to $\boldsymbol{H}$. Figure 1(b) also shows the coordinate system used for the FMR measurements. $\theta_H$ and $\theta_M$ are the angles of $\boldsymbol{H}$ and $\boldsymbol{M}$ from the [001] direction, respectively. All the samples were measured under a microwave power $P$ = 200 mW at 300 K. We note that the raw FMR spectra of all the samples included background signals, which were separately detected by measuring the FMR spectra without samples and then subtracted from the raw data [33].

In the FMR experiments, the total magnetic moment $\boldsymbol{M}$ precesses around the direction of the external magnetic field at the Larmor angular frequency $\omega$. Microwave absorption occurs when the microwave angular frequency coincides with $\omega$. This precessional motion of the magnetization is described by the well-known Landau-Lifshitz-Gilbert (LLG) equation as shown in Eq. (1),

$$\frac{1}{\gamma}\frac{\partial \boldsymbol{M}}{\partial \mathrm{t}} = -\left[\boldsymbol{M}\times(\boldsymbol{H}+\boldsymbol{H}_{\mathrm{eff}})\right]+\frac{\alpha}{(\gamma M_{\mathrm{S}})}\left[\boldsymbol{M}\times\frac{\partial \boldsymbol{M}}{\partial \mathrm{t}}\right], \tag{1}$$

where the first term on the right side shows the precessional motion of the magnetization and the second term represents damping [34],[35]. Here, $\gamma = g\mu_B/\hbar$ is the gyromagnetic ratio, where $g$, $\mu_B$, and $\hbar$ are the $g$-factor, Bohr magneton, and reduced Planck's constant, respectively, and $\alpha = \frac{G}{\gamma M_S}$ is the damping coefficient, where $G$ and $M_S$ are the Gilbert coefficient and saturation

magnetization, respectively; $\boldsymbol{H}_{\text{eff}}$ represents the effective magnetic field which includes the rf microwave magnetic field, the demagnetizing field (shape anisotropy field), and the magnetocrystalline anisotropy field. To determine the FMR condition, we used the first term of Eq. (1). In our case, the free energy density $E$ is expressed as the summation of the magnetocrystalline anisotropy energy ($E_{\text{i}}$), the shape anisotropy energy ($E_{\text{sh}}$), and the Zeeman energy ($E_{\text{Zeeman}}$). In our model, we assumed that $E_{\text{i}}$ depends only on the out of plane magnetic-field angle ($\theta_{\text{H}}$), because the in-plane magnetic-field angle ($\Phi_{\text{H}}$) dependence of FMR was almost isotropic in all the (Ga,Fe)Sb samples (data not shown). The following Eq. (2) shows the modified expression for $E$,

$$E = E_{\text{eff}} + E_{\text{Zeeman}} = -K_{\text{eff}} \cos^2\theta_{\text{M}} - M_{\text{S}}\mu_0 H\cos(\theta_{\text{H}} - \theta_{\text{M}}) \,, \tag{2}$$

where $E_{\text{i}}$ and $E_{\text{sh}}$ are combined into the effective magnetic anisotropy energy $E_{\text{eff}}$ (=$E_{\text{i}}$ + $E_{\text{sh}}$). The corresponding effective magnetic anisotropy constants of $E_{\text{i}}$, $E_{\text{sh}}$, and $E_{\text{eff}}$ are denoted as $K_{\text{i}}$, $K_{\text{sh}}$, and $K_{\text{eff}}$ (=$K_{\text{i}}$ + $K_{\text{sh}}$), respectively. $K_{\text{sh}}$ is given in Eq. (3).

$$K_{\text{sh}} = -\frac{1}{2}\mu_0 M_{\text{S}}^2. \tag{3}$$

From Eq. (2), the in-plane (perpendicular) magnetic anisotropy corresponds to negative (positive) signs of $K_{\text{eff}}$ [34],[36]. The resonance field ($\mu_0 H_{\text{R}}$) of the FMR spectrum is determined by the resonance condition given by the Smith-Beljers relation [37],[38] expressed as Eq. (4).

$$\left(\frac{\omega}{\gamma}\right)^2 = \frac{1}{(M_{\text{S}} \sin\theta_{\text{M}})^2}\left[\frac{\partial^2 E}{\partial\theta_{\text{M}}^2}\frac{\partial^2 E}{\partial\Phi_{\text{M}}^2} - \left(\frac{\partial^2 E}{\partial\theta_{\text{M}}\partial\Phi_{\text{M}}}\right)^2\right], \tag{4}$$

where $\Phi_M$ is defined as the in-plane magnetic-field angle [33]. Here, $\theta_M$ and $\Phi_M$ at the resonance condition are determined by the two equations of $\partial E/\partial\theta_M = 0$ and $\partial E/\partial\Phi_M = 0$. However, in our case, because the dependence of FMR on $\Phi_M$ was almost isotropic, we used only $\partial E/\partial\theta_M = 0$. Using Eq. (2), this condition is expressed as Eq. (5).

$$\sin(2\theta_M) = \left(2\mu_0 H_R/\mu_0 M_{eff}\right)\sin(\theta_M - \theta_H). \quad (5)$$

Here, $\mu_0 M_{eff}$ is the effective magnetic field which is expressed as $\mu_0 M_{eff} = \mu_0 M_S - H_i$, where $H_i = \frac{2K_i}{M_S}$ is the magnetocrystalline anisotropy field. From Eqs. (2) and (4), we obtained the following fitting equation [33].

$$\left(\frac{\omega}{\gamma}\right)^2 = \left[\mu_0 H_R \cos(\theta_H - \theta_M) - \mu_0 M_{eff}\cos^2\theta_M\right] \times \left[\mu_0 H_R \cos(\theta_H - \theta_M) - \mu_0 M_{eff}\cos 2\theta_M\right]. \quad (6)$$

Eqs. (5) and (6) were simultaneously solved numerically to obtain the theoretical value of $\mu_0 H_R$ and $\theta_M$, where $\gamma$ (or $g$-factor) and $\mu_0 M_{eff}$ are fitting parameters. Using the $\mu_0 M_s$ values obtained from the SQUID measurements, we first estimated $K_{sh}\left(= -\frac{1}{2}\mu_0 M_S^2\right)$, and then estimated $K_i$ $\left(= -\frac{M_S H_i}{2}, \text{where } H_i = \mu_0 M_S - \mu_0 M_{eff}\right)$. Finally, $K_{eff}$ (= $K_i$ + $K_{sh}$) was estimated for all the samples.

# IV. Results and discussions

The FMR spectra of the (Ga,Fe)Sb layers in samples A–D measured at room temperature (300 K) are shown in Figs. 6(a)–6(d), where the data obtained with ***H***//[110] and ***H***//[001] are

represented by open red circles and open black squares, respectively. In all the samples for both magnetic-field directions, we observed clear FMR signals from the (Ga,Fe)Sb thin films at room temperature. We note that the FMR signal at room temperature has never been reported for other III-V FMSs. The resonance field $\mu_0 H_R$ of the FMR spectra measured with $\boldsymbol{H}$ // [110] is smaller than that with $\boldsymbol{H}$ // [001] in all the samples, indicating that the easy magnetization axis is always in the film plane (in-plane magnetic anisotropy). This result is consistent with the SQUID results shown in Sec. II. We also note that the linewidth of the FMR spectra becomes broader from 31 mT (Sample A) to 56 mT (Sample D) for $H$ // [001] as shown in Fig. 7 (black solid circles) when the strain is changed from tensile (sample A) to compressive (sample D). This increase in FMR linewidth is attributed to the degradation of the crystal quality of the films due to the buffer layer, which also causes the decrease in saturation magnetization as shown in Fig. 7 (blue solid squares). Next, we measured the FMR spectra for various directions of $\boldsymbol{H}$ between the direction normal to the film plane ($\boldsymbol{H}$ // [001]) and the in-plane direction ($\boldsymbol{H}$ // [110]). The detailed angular dependence of $\mu_0 H_R$ on the $\boldsymbol{H}$ direction ($\theta_H$) of all the samples are represented as the black solid circles in Figs. 6(e)–6(h). The $\mu_0 H_R$ value decreased smoothly with increasing $\theta_H$ from 0° ($\boldsymbol{H}$ // [001]) to 90° ($\boldsymbol{H}$ // [110]). The change of $\mu_0 H_R$ when $\boldsymbol{H}$ is rotated from [001] to [110] monotonously decreases when one goes from sample A (0.14 T) to sample D (0.05 T). This result reflects the different MA in these samples, likely due to the different epitaxial strains. On the other hand, $\mu_0 H_R$ remained almost unchanged when we rotated $\boldsymbol{H}$ in the film plane (data not shown), indicating very weak in-plane magnetic anisotropy of the (Ga,Fe)Sb thin films. The fittings (black solid curves) reproduce the observed angular dependence of the FMR fields quite well for all the samples, as shown in Figs. 6(e)–6(h). The fitting parameters ($\mu_0 M_{eff}$ and $g$-factors) that were obtained from the fitting to the experimental $\mu_0 H_R$ data are listed in Table I.

In Table I, one can see that $\mu_0 M_{eff}$ tends to decrease when the strain is changed from tensile (sample A) to compressive (sample D). This means that $\mu_0 M_{eff}$ which carries information of the magnetocrystalline anisotropy depends strongly on the epitaxial strain of the (Ga,Fe)Sb thin film. Figures 8 (a)–(c) summarize the estimated values of magnetocrystalline anisotropy constant $K_i$, shape anisotropy constant $K_{sh}$, and effective magnetic anisotropy constant $K_{eff}$ (= $K_i + K_{sh}$), as a function of $\varepsilon$. In all the samples, the magnitude of $K_{sh}$ is one or two orders of magnitude larger than $K_i$, indicating the dominance of the shape magnetic anisotropy in the MA properties of (Ga,Fe)Sb. The strong shape anisotropy is due to the large $\mu_0 M_S$ of (Ga,Fe)Sb even at room temperature.

The magnetocrystalline anisotropy constant $K_i$, though small, shows a systematic dependence on the strain $\varepsilon$. As shown in Fig. 8(a), when the strain is changed from tensile ($\varepsilon$ = –1.7%) to compressive ($\varepsilon$ = +3.84%), the magnitude of $K_i$ increases and changes from negative (in-plane anisotropy) to positive (perpendicular anisotropy). These results indicate that it is feasible to control the magnetocrystalline anisotropy of (Ga,Fe)Sb thin films by using epitaxial strain. Meanwhile, $K_{sh}$ is always negative as shown in Fig. 8(b), making $K_{eff}$ always negative (in-plane magnetic anisotropy) as shown in Fig. 8(c). As a result, all the (Ga,Fe)Sb thin films examined here have in-plane magnetic anisotropy. These results of (Ga,Fe)Sb are contrasting to those of (Ga,Mn)As in the following two points: (i) In (Ga,Mn)As, $K_i$ is large (magnetocrystalline field $H_i$ is ~ several 1000 Oe [20]) and dominates MA, but (Ga,Fe)Sb shows small $H_i$ ~ 100–300 Oe (listed in Table I) and possesses a very large $K_{sh}$. (ii) In (Ga,Mn)As compressive (tensile) strain leads to in-plane (perpendicular) magnetic anisotropy, but in (Ga,Fe)Sb tensile (compressive) strain leads to in-plane (perpendicular) magnetic anisotropy, thus the strain effect is opposite.

Therefore in (Ga,Fe)Sb, the shape anisotropy should be utilized to control the in-plane magnetic anisotropy.

## V. Conclusion

We have successfully grown a series of (Ga,Fe)Sb thin films with the Fe concentration of 20% on different buffer layers, AlSb, GaSb, $In_{0.5}Ga_{0.5}As$, and GaAs, which all exhibit room-temperature ferromagnetism. The epitaxial strain $\varepsilon$ in the (Ga,Fe)Sb layers was gradually varied over a wide range from –1.7% (tensile strain) to +3.84% (compressive strain). We observed clear FMR signals in (Ga,Fe)Sb at room temperature (this is the first observation of FMR in III-V based FMSs at room temperature), and determined the magnetic anisotropy constants. We found that the magnitude of $K_i$ is weak and shows a monotonous dependence on the strain. By changing the strain from tensile to compressive, $K_i$ changed from negative (in-plane magnetic anisotropy) to positive (perpendicular magnetic anisotropy). Meanwhile, $K_{sh}$ was always negative and is dominant over $K_i$, leading to negative $K_{eff}$ (in-plane magnetization) in all the samples. This study suggests that the easy magnetization axis of (Ga,Fe)Sb can be controlled by changing the shape anisotropy.

**ACKNOWLEDGMENTS**

This work was partly supported by Grants-in-Aid for Scientific Research (No. 18H03860, No. 17H04922 and No. 16H02095), CREST of JST (JPMJCR1777), the Spintronics Research Network of Japan (Spin-RNJ), and Murata Science Foundation.

## REFERENCES


[1] M. Oestreich, J. Hubner, D. Hagele, P. J. Klar, W. Heimbrodt, W. W. Ruhle, D. E. Ashenford, and B. Lunn, Appl. Phys. Lett. **74**, 1251 (1999).

[2] M. Oestreich, Nature **402**, 735 (1999).

[3] S. Ghosh, and P. Bhattacharya, Appl. Phys. Lett. **80**, 658 (2002).

[4] Y. Chye, M. E. White, E. Johnston-Halperin, B. D. Gerardot, D. D. Awschalom, and P. M. Petroff, Phys. Rev. B **66**, 201301, (2002).

[5] L. Chen, F. Matsukura, and H. Ohno, Nat. Commun. **4**, 2055 (2013).

[6] H. Ohno, Science (Washington, DC, U.S.) **281**, 951 (1998).

[7] M. Tanaka, J Cryst Growth **278**, 25 (2005).

[8] S. Ikeda, J. Hayakawa, Y. M. Lee, F. Matsukura, Y. Ohno, T. Hanyu, & H. Ohno, IEEE Trans. Electron Devices, **54**, 991(2007).

[9] For a detailed review see H. Ohno, J. Magn. Magn. Mater. **200**, 110 (1999).

[10] S. Datta and B. Das, Appl. Phys. Lett, **56**, 665 (1990).

[11] S. Sugahara, M. Tanaka, Appl. Phys. Lett. **84**, 2307 (2004).

[12] L. Chen, X. Yang, F. Yang, J. Zhao, J. Misuraca, P. Xiong, and S. Von Molnár, Nano Lett. **11**, 2584 (2011).

[13] P. N. Hai, L. D. Anh, S. Mohan, T. Tamegai, M. Kodzuka, T. Ohkubo, K. Hono, and M. Tanaka, Appl. Phys. Lett. **101**, 182403 (2012).

[14] P. N. Hai, L. D. Anh, and M. Tanaka, Appl. Phys. Lett. **101**, 252410 (2012).

[15] P. N. Hai, D. Sasaki, L. D. Anh, and M. Tanaka, Appl. Phys. Lett. **100**, 262409 (2012)

[16] N. T. Tu, P. N. Hai, L. D. Anh, and M. Tanaka, Appl. Phys. Lett. **112**, 122409 (2018).

[17] L. D. Anh, D. Kaneko, P. N. Hai, and M. Tanaka, Appl. Phys. Lett. **107**, 232405 (2015).

[18] N. T. Tu, P. N. Hai, L. D. Anh and M. Tanaka, Phys. Rev. B **92**, 144403 (2015).

[19] N. T. Tu, P. N. Hai, L. D. Anh, and M. Tanaka, Appl. Phys. Lett. **108**, 192401 (2016).

[20] X. Liu, Y. Sasaki, and J. K. Furdyna, Phys. Rev. B **67**, 205204 (2003).

[21] U. Welp, V. K. Vlasko-Vlasov, X. Liu, J. K. Furdyna, and T. Wojtowicz, Phys. Rev. Lett. **90**, 167206, (2003).

[22] U. Welp, V. K. Vlasko-Vlasov, A. Menzel, H. D. You, X. Liu, J. K. Furdyna, and T. Wojtowicz Appl. Phys. Lett. **85**, 260 (2004).

[23] X. Liu, W. L. Lim, M. Dobrowolska, J. K. Furdyna, and T. Wojtowicz. Phys. Rev. B **71**, 035307, (2005).

[24] C. Bihler, H. Huebl, and M. S. Brandt, Appl. Phys. Lett. **89**, 012507 (2006).

[25] D. Y. Shin, S. J. Chung, Sanghoon Lee, X. Liu, and J. K. Furdyna. Phys. Rev. B **76**, 035327 (2007).

[26] H. Son, S. J. Chung, S. Y. Yea, S. Lee, X. Liu and J. K. Furdyna, J. Appl. Phys. **103**, 07F313, (2008).

[27] S. Kim, H. Lee, T. Yoo, S. Lee, S. Lee, X. Liu and J. K. Furdyna, J. Appl. Phys. **107**, 103911, (2010).

[28] H. Terada, S. Ohya, Y. Iwasa, and M. Tanaka, Sci. Rep. **7**, 5618, (2017).

[29] A. Shen, F. Matsukura, Y. Sugawara, T. Kuroiwa, H. Ohno, A. Oiwa, A. Endo, S. Katsumoto, and Y. Iye, Appl. Surf. Sci, **113**, 183 (1997).

[30] P. T. Chiu, S. J. May and B. W. Wessels, J. Appl. Phys., **99**, 083907, (2006).

[31] Y. Yuan, Y. Wang, K. Gao, M. Khalid, C. Wu, W. Zhang, F. Munnik, E. Weschke, C. Baehtz, W. Skorupa, and M. Helm, J. Phys. D **48**, 235002 (2015).

[32] B. Heinrich, and J. F. Cochran, Adv. in Phys. **42**, 15 (1993).

[33] See Supplemental Material at [URL will be inserted by publisher] for additional descriptions and supplementary data.

[34] M. Farle, Rep. Prog. Phys. **61**, 755 (1998).

[35] C. Kittel, Phys. Rev. **73**, 155 (1948).

[36] M T Johnson, P. J. H. Bloemen, F. J. A. Den Broeder, and J. J. De Vries, Rep. Prog. Phys. **59**, 1409 (1996).

[37] J. Smith, and H.G. Beljers, Phillips, Res. Rep. **10**, 113 (1955).

[38] X. Liu, and J.K. Furdyna, J. Phys. Condens. Matter, **18**, R245 (2006).

[39] G. Giesecke and H. Pfister, Acta Crystallogr. **11**, 369 (1958).

[40] D. T. Bolef and M. Menes, J. Appl. Phys. **31**, 1426 (1960).

[41] W. F. Boyle and R. J. Sladek, Phys. Rev. B **11**, 2933 (1975).

TABLE I. Epitaxial strain ($\varepsilon$) estimated from XRD, saturation magnetization ($\mu_0 M_s$) measured by SQUID, effective magnetization ($\mu_0 M_{eff}$), magnetocrystalline anisotropy field ($H_i$), and $g$-factor obtained by the fitting to the FMR spectra of $(Ga_{0.8},Fe_{0.2})Sb$ in samples A–D with different buffer layers.

| Sample | Buffer | $\varepsilon$ (%) | $\mu_0 M_S$ (mT) | $\mu_0 M_{eff}$ (mT) | $H_i$ (Oe) | $g$-factor |
|---|---|---|---|---|---|---|
| A | AlSb | –1.7 | 89.9 | 104.3 + 0.5 | -144 + 5 | 2.08 + 0.03 |
| B | GaSb | –0.1 | 77.9 | 90.4 + 0.1 | -125 + 1 | 2.07 + 0.03 |
| C | $In_{0.5}Ga_{0.5}As$ | +0.23 | 59.8 | 37.1 + 0.2 | 227 + 2 | 2.1 + 0.03 |
| D | GaAs | +3.84 | 66.3 | 32.3 + 0.2 | 340 + 2 | 2.11 + 0.03 |

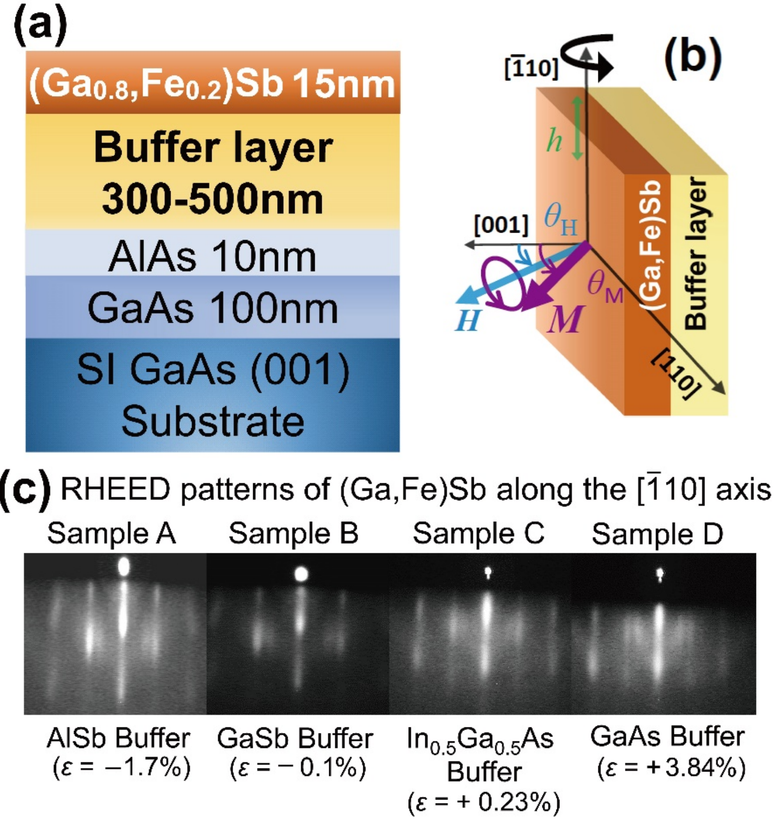


FIG. 1. (a) Schematic illustration of the (001)-oriented sample structure composed of $(Ga_{1-x}Fe_x)Sb$ grown on different buffer layers on a semi-insulating GaAs(001) substrate. (b) Sample alignment and coordinate system used in the ferromagnetic resonance (FMR) measurement system. A radio-frequency (rf) magnetic field $h$ was applied along the $[\bar{1}10]$ direction of the sample. $\theta_H$ and $\theta_M$ are the angles of the magnetic field $\boldsymbol{H}$ and the magnetization $\boldsymbol{M}$ with respect to the [001] direction, respectively. (c) *In-situ* reflection high energy electron diffraction (RHEED) patterns observed along the $[\bar{1}10]$ axis during the MBE growth of the 15-nm-thick (Ga,Fe)Sb thin films on AlSb (Sample A), GaSb (Sample B), $In_{0.5}Ga_{0.5}As$ (Sample C), and GaAs (Sample D) buffer layers.

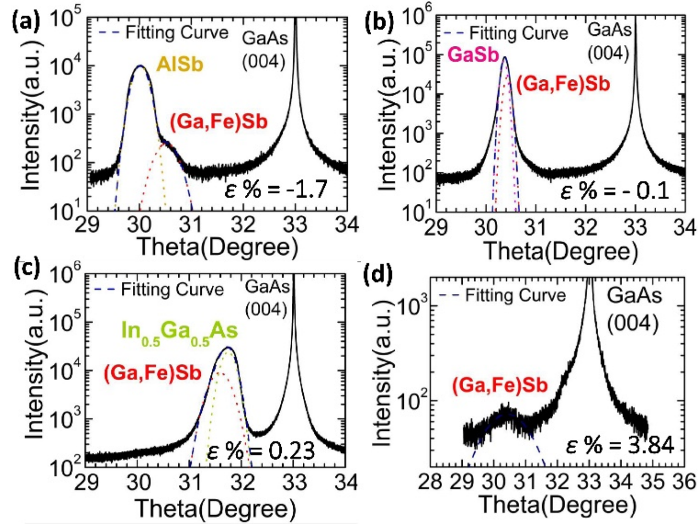


FIG. 2. (a)–(d) X-ray diffraction rocking curves of samples A–D. The broad peak in sample A–C was fitted by the Gaussian curves corresponding to the peaks of the (Ga,Fe)Sb thin film (red dotted line) and of the buffer layers of AlSb (yellow dotted line) (a), GaSb (pink dotted line) (b), and $In_{0.5}Ga_{0.5}As$ (green dotted line) (c). The sum of the two curves is the fitting curve which is plotted by the violet dashed line. In sample D, the (Ga,Fe)Sb (004) peak (blue-violet dashed line) can be clearly seen. For each sample, the epitaxial strain ($\varepsilon$ %) was estimated [33] and shown in the figure.

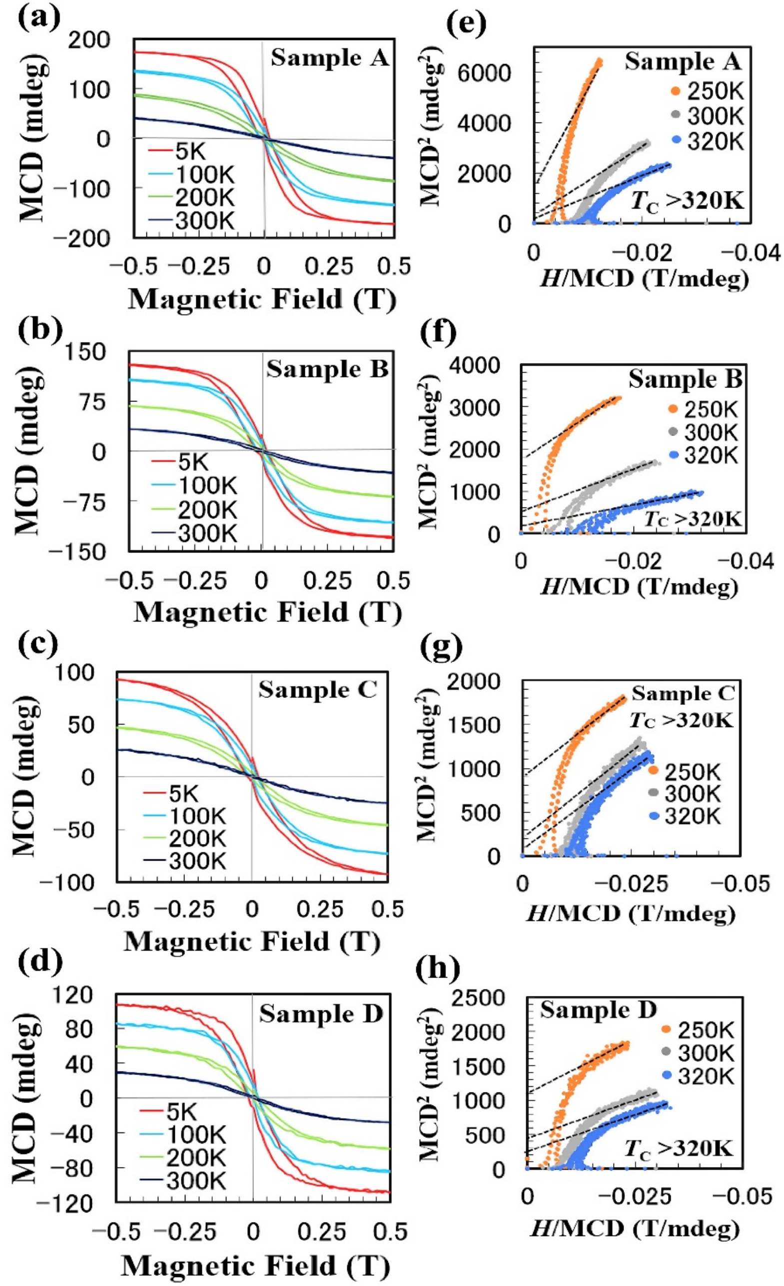


FIG. 3. (a)–(d) MCD-*H* curves at different temperatures, (e)–(h) Arrott plots of $(Ga_{0.8}Fe_{0.2})Sb$ grown on different buffer layers. The (Ga,Fe)Sb thin films in all the samples exhibit clear ferromagnetism with $T_C > 320$ K.

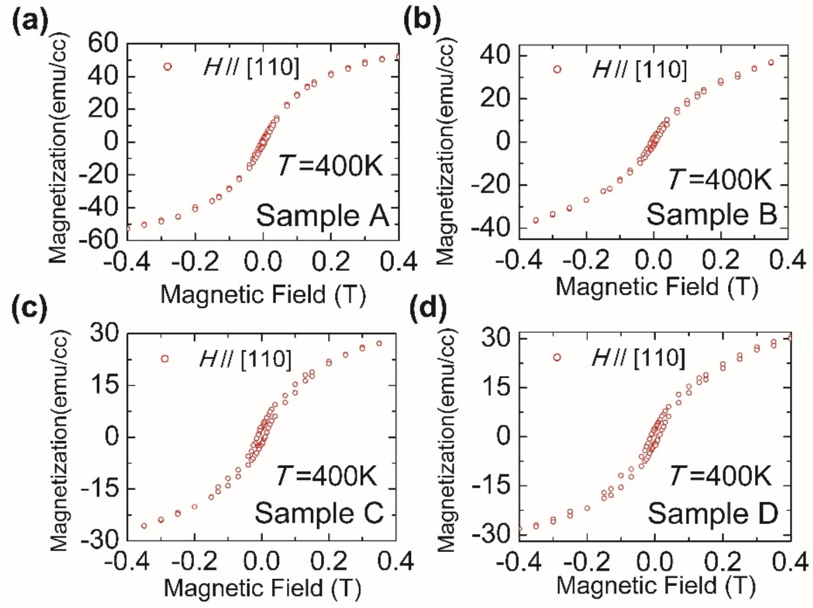


FIG. 4. (a)–(d) Magnetization hysteresis curves (*M*-*H*) measured at 400 K for ($Ga_{0.8}$,$Fe_{0.2}$)Sb grown on the AlSb (a), GaSb (b), $In_{0.5}Ga_{0.5}As$ (c), and GaAs (d) buffer layers when the magnetic field was applied in the film plane along the [110] axis (red open circles). These characteristics show that the $T_C$ of these ($Ga_{0.8}$,$Fe_{0.2}$)Sb is higher than 400 K.

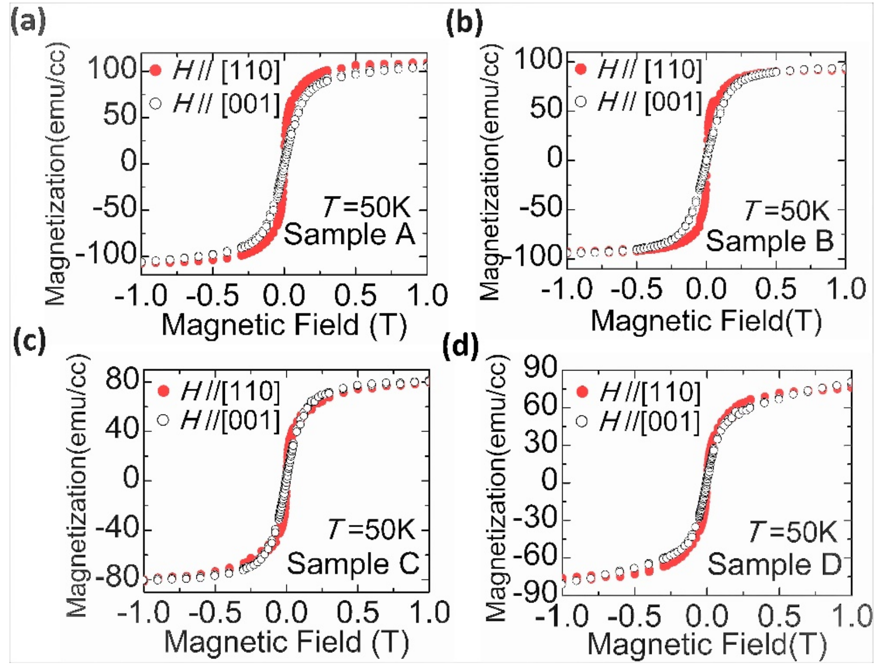


FIG. 5. (a)–(d) Magnetization hysteresis curves (*M*-*H*) measured at 50 K for $(Ga_{0.8},Fe_{0.2})Sb$ grown on the AlSb (a), GaSb (b), $In_{0.5}Ga_{0.5}As$ (c), and GaAs (d) buffer layers when the magnetic field was applied in the film plane along the [110] axis (red solid circles) and perpendicular to the plane along the [001] axis (black open circles).

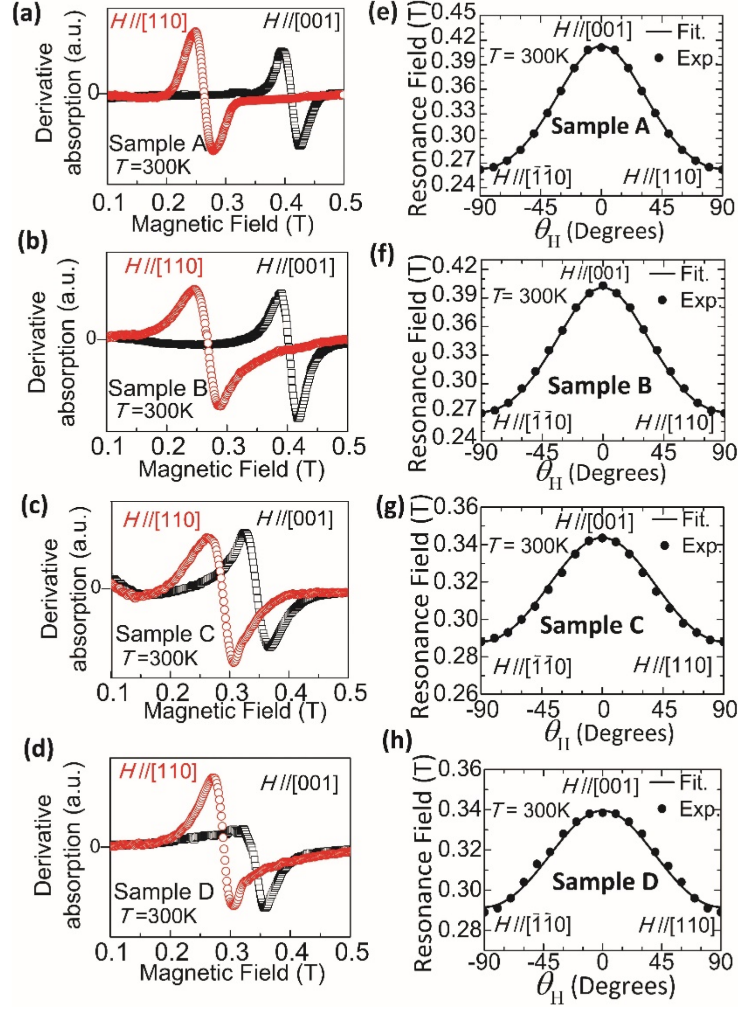


FIG. 6. (a)–(d) FMR spectra observed for $(Ga_{0.8},Fe_{0.2})Sb$ on the AlSb (a), GaSb (b), $In_{0.5}Ga_{0.5}As$ (c), and GaAs (d) buffer layers at room temperature (300 K) when the magnetic field $H$ was applied along [110] ("red" circles) and [001] ("black" squares). (e)–(h) Resonance field $\mu_0 H_R$ as a function of the direction angle $\theta_H$ of $\mu_0 H$.

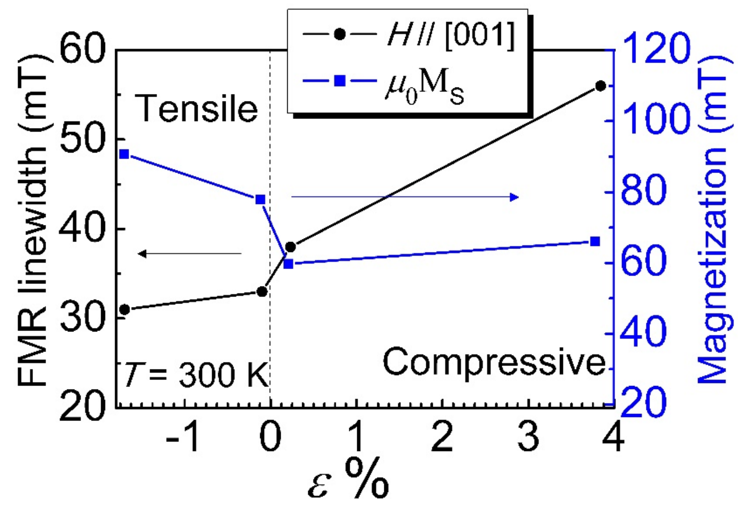


FIG. 7. FMR linewidth when the magnetic field is applied along [001] (black solid circles) and the saturation magnetization (blue solid squares) *vs.* strain ($\varepsilon$).

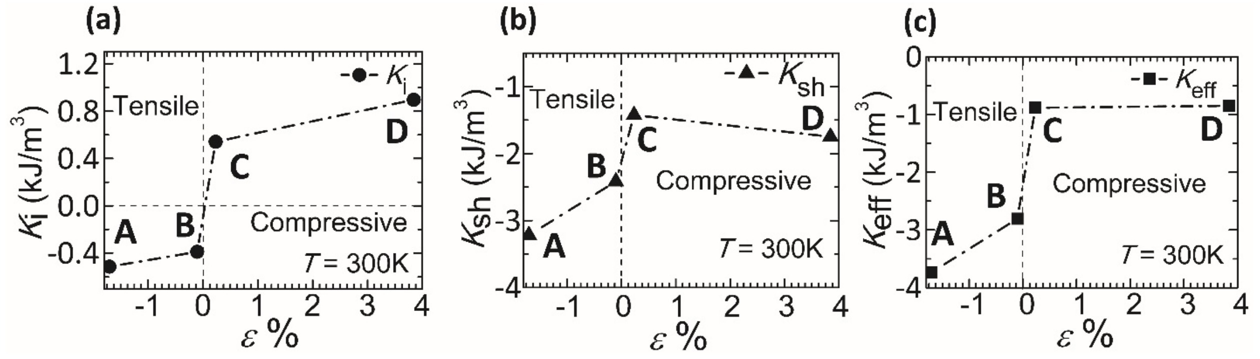


FIG. 8. (a)–(c) Strain ($\varepsilon$) dependence of the magnetocrystalline anisotropy constant $K_i$ (a), shape anisotropy constant $K_{sh}$ (b), and effective magnetic anisotropy constant $K_{eff}$ (c) of (Ga,Fe)Sb thin films grown on different buffer layers.